Materials Characterization 170 (2020) 110673

Contents lists available at ScienceDirect

Materials Characterization

journal homepage: www.elsevier.com/locate/matchar

Quantification of strain fields and grain refinement in Ti-6Al-4V inter-pass rolled wire-arc AM by EBSD misorientation analysis

A.E. Davis [a,*], J.R. Hönnige [b,1], F. Martina [b], P.B. Prangnell [a]

[a] Department of Materials, University of Manchester, Manchester M13 9PL, UK
[b] Welding Engineering and Laser Processing Centre, Cranfield University, Cranfield MK43 0AL, UK

ARTICLE INFO

Keywords:
Titanium
Deformation
Electron backscatter diffraction
Additive manufacturing

ABSTRACT

Inter-pass deformation is an effective method for refining the coarse β-grain structure normally produced in high-deposition-rate additive manufacturing processes, like wire-arc additive manufacturing. The effectiveness of applying contoured surface rolling deformation tracks to each added layer has been studied by developing, and applying, a large-area SEM-based strain mapping technique. This technique is based on calibration of the average point-to-point Local Average Misorientation (LAM) of α-phase lamellar variants in EBSD orientation data to the local effective plastic strain. Although limited in the strain range that can be measured, the technique has proven to be very effective for identifying the size and depth of the plastic zone induced by surface rolling, as well as the local strain distribution, up to a saturation limit of ~12%. The strain fields mapped showed a close correlation to the region and level of recrystallization that occurred in the deformation zones during rapid re-heating through the β transus. The β recrystallization identified was consistent with the local strain distribution within the plastic zones measured by the LAM method and previous work on the recrystallization mechanisms operating in WAAM inter-pass deformation processes.

1. Introduction

High deposition rate additive manufacturing (AM) processes, like Wire-Arc AM (WAAM), have the ability to deposit large near-net-shape components, at rates of kilograms-per-hour, with build envelopes of several metres, and short lead times [1,2]. Using such directed energy deposition (DED) processes, to produce titanium aerospace components, offers significant cost savings, due to the inherently expensive material, tooling, and machining operations involved in manufacturing conventional wrought components [1,3]. In order to achieve high deposition rates, wire-based AM technologies, such as WAAM, employ a high energy heat source and produce larger melt pools, which result in lower cooling rates than in powder bed processes [4,5]. In Ti alloys like Ti-6Al-4V (Ti64), these solidification conditions, combined with restricted constitutional undercooling and a lack of inoculation, result in the formation of large columnar β grains – often cm's in size – that grow epitaxially upwards from the fusion boundary in each layer, and exhibit a strong $<001>_{\beta}$ fibre texture aligned approximately normal to the rear melt pool surface [6–10]. Even though this strong β solidification texture is weakened upon cooling, because α nucleates with 12 possible variant orientations governed by the Burgers orientation relationship (BOR) [11], the large parent columnar β grains have been shown to be detrimental to mechanical properties [8,12–15]. Fortunately, the coarse β grains formed on solidification in Ti64 WAAM components can be refined by either: intelligent control of the thermal conditions during deposition [6], alloy modification (e.g. Si [16] and Ti-Al-Nb [17,18]), or by exploiting inter-pass deformation techniques, such as machine hammer peening [19–21] and rolling [7–9].

In WAAM with inter-pass deformation, the deposited material is rolled or peened between each heat source pass, when the material has cooled below the β transus [8,9,21–24]. This cycle of material deposition, cold work, and the subsequent rapid re-heating on deposition of the next layer, has been shown to produce an unexpectedly high level of grain refinement and texture randomisation in Ti64 WAAM deposits, by disrupting the detrimental columnar β-grain structure [7–9,19–21,23,25]. The recrystallized (RX) microstructure consists of small, equiaxed grains, separated by high angle grain boundaries (HAGBs), and exhibits a markedly weakened texture when compared to the conventional WAAM $<001>_{\beta}$ fibre texture [7–9,19–21,25]. The discovery of this high level of grain structure refinement in Ti64 during

* Corresponding author.
E-mail address: alec.davis@manchester.ac.uk (A.E. Davis).
[1] Now at: Premium Aerotec, Premium AEROTEC GmbH, Riesweg, 151–155, 26316 Varel, Germany.

https://doi.org/10.1016/j.matchar.2020.110673
Received 12 May 2020; Received in revised form 22 September 2020; Accepted 23 September 2020
Available online 25 September 2020

inter-pass deformation is surprising, as only relatively small strains [7,8,25] are required when compared with processing conventional wrought products [26,27]. It has been suggested by the current authors that this grain refinement effect may be caused by a novel RX mechanism that can operate in inter-pass deformed WAAM materials, due to their fine transformation microstructure and the rapid heating conditions, that involves twinning of the deformed β phase during its re-growth on re-heating through the β transus [28]. Henceforth, this mechanism will therefore be referred to as *rapid-heating β RX*. Furthermore, it has recently been shown that rapid-heating β RX initiates for applied strains as low as ~9%, but that the level of refinement rapidly reaches a lower limit and saturates at strains above ~14% [25].

To be able to optimise the application of inter-pass deformation technologies in AM, it is therefore important to understand the sub-surface strain distribution each method induces and, in particular, its intensity as a function of the strain field penetration relative to the re-melt depth. Quantified strain mapping in metals can be experimentally achieved by several methods; which include direct surface displacement measurement methods, such as digital image correlation (DIC), whereby speckle patterns [29–36] or microstructural features [35–38] are tracked during deformation; and indirect methods that measure changes to the deformed microstructure induced by plastic strain. The majority of the indirect approaches are based on interpretation of Electron Backscatter Diffraction (EBSD) data, which can be processed to determine inter-granular crystal misorientations, or changes in pattern quality, that can then be used to estimate the local plastic strain by interpretation of the inferred dislocation density or from the lattice distortion [39–42]. However, DIC techniques can only be applied to a free surface, which will be in a different strain state and cannot be easily utilised in the case of surface rolling due to the geometry restrictions. The application of EBSD-based methods to AM materials is also challenging because of the complex fine-scale lamellar α + β Ti microstructure, which contains no real 'grains' of the dominant α phase, in the conventional sense, but rather consists of multi-variant (basket-weave) α lamellar colonies (e.g. [35,36,43,44]), with plate dimensions of ~1 μm in width, by 3–5 μm long. To perform the conventional approaches, high resolution EBSD analysis is therefore required, which, with the speed of current systems, would restrict the possible mapping area to $< \sim 1$ mm^2. Alternatively, the strain distribution could be *inferred* from micro-hardness mapping [45], but this is unreliable in α + β Ti alloys as the local yield stress is highly sensitive to micro-texture grain orientations (such as α colonies) and WAAM deposited Ti64 has a low strain hardening rate [8,12,24,46]; as a consequence, hardness mapping has low spatial and strain resolution. Finite element (FE) modelling has been applied to inter-pass surface rolling in the WAAM process to predict the effect on the residual stresses [47]. However, FE requires validation and key boundary conditions must be assumed – such as the contact friction – and it does not take into account micro-texture effects caused by the heterogeneous and coarse β-grain microstructures.

In the current work, in order to aid optimisation of Ti64 WAAM inter-pass deformation technologies, a local orientation-based EBSD strain characterisation measurement method [40] has, therefore, been adapted for application to mapping large areas in a fine α basket-weave transformation microstructure. When calibrated against samples subjected to a known plastic strain, to produce quantified strain maps, the method was found to be sufficiently sensitive to the strain range where the rapid-heating β RX refinement starts to operate in Ti64. The technique was based on obtaining high quality patterns during EBSD mapping of deformed samples with a relatively large step size, that were subsequently processed to obtain local orientation data for single variants within the α phase. The orientation data was then converted into local average misorientation (LAM) maps, which calculated the average misorientation in an 11 × 11 kernel, across multiple lamellae from α variants within individual colonies in the microstructure. The local strain was then determined by calibration against plane strain compression (PSC) test samples, using the same material, for which FE modelling was used to calculate the strain distribution. This approach was adopted as it was found to be able to effectively (and simply) map strain fields over large areas (i.e. cm^2) in the strain interval of interest, without requiring prohibitively large datasets. Furthermore, it allowed the strain fields produced in inter-pass rolled WAAM components to be successfully identified, quantified, and the depth and degree of β refinement to be reliably predicted.

2. Materials and methods

2.1. WAAM samples

The strain-mapping technique developed (§2.4) was applied to a typical WAAM component, that was deposited using a 'parallel' build strategy, with the process parameters provided in Table 1 (more details can be found in ref. [48]). With this build strategy, three tracks with a 50% overlap were deposited in parallel for each deposited layer. The wall was subsequently machined to a thickness of 15 mm. The sample reference frame was defined as: WD = the wall, or deposition track translation direction, TD = the wall transverse direction, and ND = the layer normal, or build-height direction. To attempt to characterise the strain field produced, and thereby investigate the effectiveness of surface rolling, the WAAM wall was subjected to deformation by rolling at room temperature, at a speed of 6 mm s^{-1}, with a 150 mm diameter steel roller with a convex profiled surface of 3 mm radius. The wall was rolled on its *side* surfaces, with the rolling direction parallel to WD and the compression direction parallel to TD, using widely spaced tracks to remove any potential effects from the reduced constraint on rolling near an edge, or effects from roll-track overlap. After examination in the as-rolled condition, small ~6 × 6 × 6 mm samples were removed below the surface symmetrically around each rolled track. Some samples were prepared for metallographic and EBSD analysis. Other specimens were β annealed by rapid induction heating at a rate of ~600 °C s^{-1}, to replicate a typical WAAM thermal cycle (e.g. [43]), and were immediately gas quenched using a TA Instruments DIL 805A/D/T quench-dilatometer. With this large size of specimen, the high heating rate could only be achieved by using the dilatometer at 100% power, which introduced ±20 °C uncertainty into the target temperature. Thus, the samples were heated to ~1175 °C, to ensure the material fully transformed to β.

Hardness maps were generated on metallographically prepared samples, polished to an optical finish (see below), using a Struers Durascan 80 auto-hardness tester, to produce an array of indents with a 150 μm spacing with an applied load of 0.1 kg.

2.2. Plane strain compression tests

To calibrate the orientation measurements against a known compressive strain, PSC tests were conducted at room temperature on 5 mm^3 Ti64 WAAM cubes, cut from the steady-state region of a single-bead-wide WAAM wall (details given in ref. [25]). The samples were compressed in a purpose-built PSC rig (shown in Fig. 2a) using an Instron Universal Testing Machine 5569H with a 50 kN load cell. The PSC tooling and sample cubes were coated in a graphite-based lubricant and were strained at 0.5 mm s^{-1}, to a range of reduction ratios between 7 and 20%. The resultant strain distributions within these samples were

Table 1
WAAM deposition parameters [48].

Heat source parameters		Gas flow rates	
Current	180 A	Plasma gas	0.8 l/min
Work piece distance	8 mm	Plasma shield	8 l/min
Travel speed	0.4 m/min		
Wire feed rate	2.4 m/min		
Wire diameter	1.2 mm		

estimated using an FE model that used the sample shape change to replicate the tool-die friction effects, using the commercial software package QForm [25].

Samples for optical and EBSD examination were sectioned in their ND-TD plane and metallographically prepared using SiC paper, with decreasing coarseness to 4000 grit, followed by polishing with an OPS and 5% concentrated hydrogen peroxide solution. Following etching in Kroll's Reagent, optical images were taken using a Zeiss Axio Imager 2, to create large area high-resolution images using automated stitching software. SEM was conducted in an FEI Magellan FEG-SEM, using a 5 kV accelerating voltage, a 1.6 nA current, and a working distance of 5 mm. Automated α inter-lamellar spacings were measured from backscatter electron SEM micrographs with purpose-built software, which uses the standard linear intercept method and corrects for diagonally-orientated lamellae [49].

2.3. EBSD mapping

EBSD orientation maps were obtained using an FEI Sirion FEG-SEM equipped with a Nordlys Nano EBSD detector and Oxford Instruments' AZtec software, at a 20 kV accelerating voltage. For standard maps, electron backscatter patterns (EBSPs) were collected using 8 × 8 binning and the step size was varied depending on the required final map area. For the LAM maps, EBSPs were collected with a standard step size of 2 μm, using 4 × 4 binning with higher resolution patterns (336 × 256 pixels) to achieve a greater indexing rate throughout deformed regions. EBSD data was processed using Oxford Instruments' HKL Channel5 software to produce orientation maps, LAM maps, and pole figures.

To study the β-grain structure and texture, α EBSD maps were collected at a step size appropriate for the intended final map size and processed in Channel5. β-phase parent grain orientation maps were then produced by reconstruction, using the method devised by Davies and Wynne [50–53] that calculates the parent β orientations from the α-phase EBSD data through the BOR. In the reconstruction procedure, a ±2° α to parent β misorientation error for a particular α variant was accepted, and a ±3° divergence from the BOR was allowed. These maps are shown in inverse pole figure (IPF) colouring relative to the WAAM build direction (ND), and contoured pole figures are given in multiples of random density (MRD).

2.4. Local averaged misorientation (LAM) measurements

To accurately detect inter-granular misorientations within a deformed microstructure, using EBSD, the SEM beam conditions and EBSP acquisition settings have to be set to ensure high resolution EBSPs can be acquired - to ensure reliable indexing - and that sufficient pixels per grain are collected to allow kernel averaging, to reduce local misorientation noise and maximise the orientation resolution [40]. If these conditions are met, properties like LAM, which measures the misorientation between pixels in an EBSD map between neighbouring kernels of a pre-determined size, can be calculated to an accuracy of ~0.5–1^0 [54]. In Ti64 WAAM, where the α lamellae have a typical spacing of ~0.7–1 μm [43], the EBSD step size required would be <0.1 μm to produce a reliable LAM map [40] from individual α plates, which is not practical for collecting the large maps required to quantify the strain fields produced by inter-pass deformation in WAAM. For example, the strain field that we wished to characterise in the work presented here is ~3 mm deep. Even with the emerging CMOS EBSD high-speed indexing systems, such a map would take weeks to obtain, and data processing would be a significant challenge.

To overcome these technical difficulties, in this work, a new method was devised whereby a larger EBSD step size could be adopted, by taking advantage of the constrained orientation distribution that exists in Ti64 WAAM α lamellar microstructures, when the α phase transforms from large prior β grains. This results in each parent β grain containing regions of similarly orientated α lamella variants, which form from the set of 12 possible according to the BOR. The basket-weave microstructure in WAAM consists of multi-variant lamellar α *colonies,* which are of the order of ~10–100 μm in size and contain the same subset of (usually 3) neighbouring variants [55], separated by fine retained β. Examples of the measurement method employed, and the limitations involved, are provided in Fig. 1.

An enlarged section, taken from an EBSD Euler angle map from within a single prior β-grain Ti64 WAAM sample, deformed to an effective strain of ~10%, using a 2 μm step size, is presented in Fig. 1a. This small map area shows examples of the typical variant clusters found within a β grain, as seen when mapped with a 2 μm step size. A single α variant orientation from this map has been singled out in Fig. 1b (pole figure in Fig. 1c) and shows that lamellae from this variant are distributed within several colonies. With this step size, the individual lamellae have a width of at least a single pixel; thus, to infer a strain distribution by LAM mapping within a *single* α lamella is impossible at this spatial resolution. However, if the LAM kernel is enlarged so that the local orientation of multiple lamellae are averaged and included in the calculation – i.e. lamellar clusters of one variant are treated as a single grain – then statistically relevant average misorientations can be collected over a larger area. This approach is demonstrated in Fig. 1b, where a single α variant has been identified over the whole map region, by segmenting individual variants using a filter set to exclude misorientations greater than 5°. The white boxes (solid lines) shown in Fig. 1d represent an 11 × 11 kernel (22 × 22 μm), which can be seen to enclose clusters and/or colonies of the single α variant, depending on its position. This 11 × 11 kernel was selected as the optimum size that could be used to improve orientation accuracy and remove excessive noise in the measurements, without obscuring real strain gradients. As the strain field under the surface roller was of the order of 3 mm deep, measuring the local strain with a resolution of 22 μm was considered to be more than sufficient.

In Fig. 1d, the local orientations within this single variant are magnified in the range of 0–5° misorientation and the corresponding LAM map obtained for the same map region using a 5° segmentation prefilter is shown in Fig. 1e. For comparative purposes, smaller 0.3 μm step size maps from an *undeformed* material are shown in Fig. 1f–g, which depict more clearly the α lamellar boundaries, but where a greater maximum misorientation cut-off has been used of 8° in the LAM measurements. By comparison of Fig. 1b–d, it can be seen that misorientations captured by using a 5° limit are confined within the single α variant. Within the isolated single variant, there is a spread of orientations (Fig. 1b) which are detected by the LAM kernel. However in this example, at this plastic strain level, over this small distance, a ~ 2–4° kernel–kernel LAM pixel range is seen. LAM measurements from the other variants in the map in Fig. 1a also indicate that the variation between different α variant orientations is within the same range.

In the higher resolution map, taken from the undeformed sample shown in Fig. 1f, small misorientation gradients can already be seen within long α laths and also between individual plates. This is expected from small variations in the habit plane between individual α variants within the β matrix and due to misfit strains developed during the phase transformation and rapid cooling [56–59]. With kernel averaging, the accuracy of the orientation measurement is of the order of 0.5–1° [54], and when combined with misfit strains, these two effects lead to a minimum misorientation resolution below which the effect of applied plastic deformation cannot be detected in an α + β transformation microstructure. In addition, these higher resolution maps have been provided to exemplify the need for a 5° cut-off filter to isolate the misorientations developing within a specific α variant. This is necessary because two different α variants within the same parent β grain can theoretically have orientations that are within 10.5° of each other [57,58]. If such a second variant were included in a LAM kernel from a given segmented variant, it would significantly raise the average misorientation calculation, and would indicate more deformation where there was none. This would disproportionally skew the measurements in

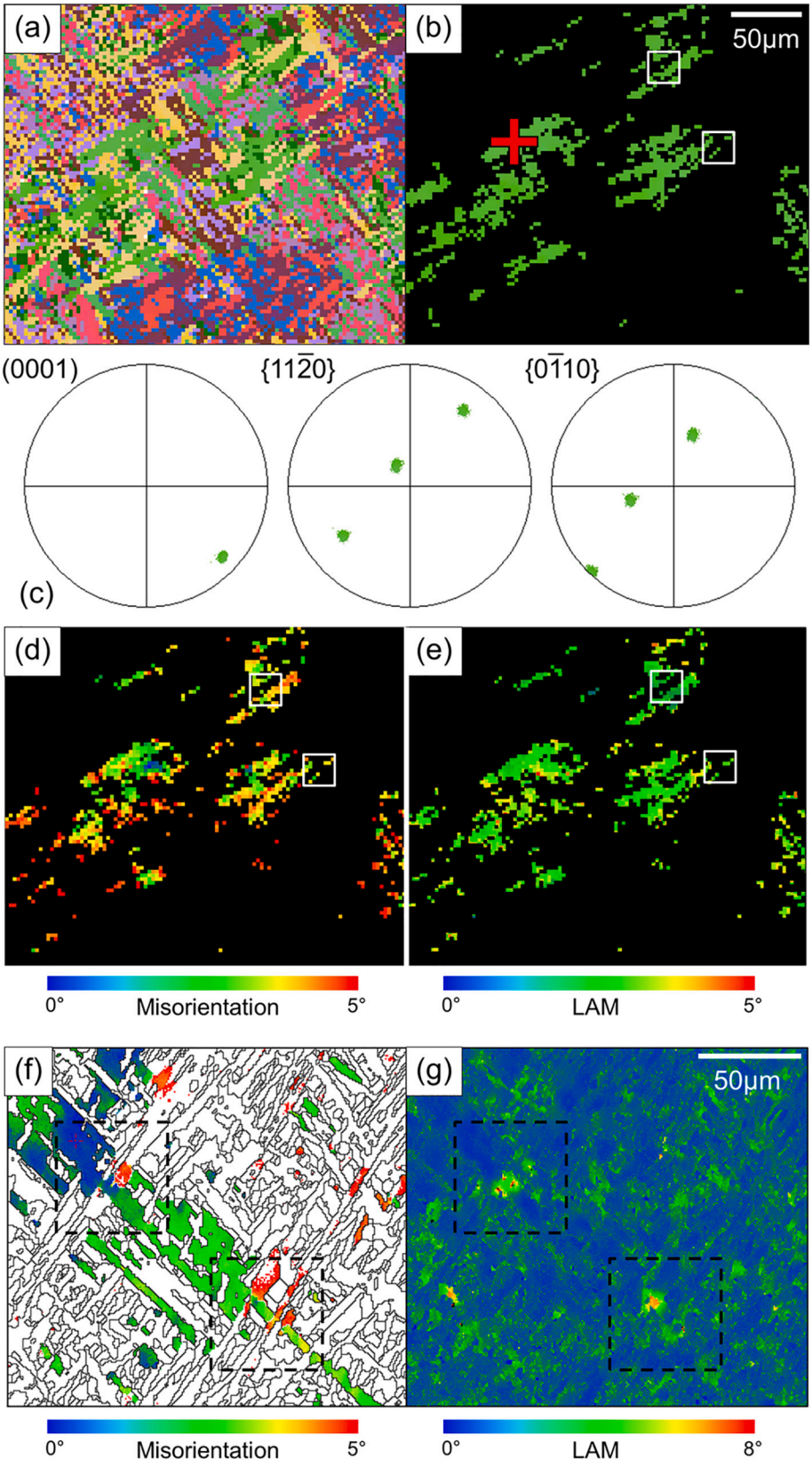

Fig. 1. A magnified small region from an EBSD map of a deformed Ti64 WAAM microstructure (effective strain ~10%), collected with a 2 μm step size, showing: (a) the map in Euler colouring, (b) after filtering to include only a single α variant orientation (marked with the red cross; misorientation spread <1°), (c) pole figures of the selected orientation, (d) a map showing the local orientations present within the range 0–5° of the selected starting orientation (shown in (b)), and in (e) the corresponding LAM map to (d) is shown with a 5° cut off. In (d-e), the white boxes give examples of where the same single-variant α lamellae are contained within a single kernel in two different colonies. In (f), the orientations within an 8° range from a selected starting variant are shown (similar to (d)) using a smaller step size (0.3 μm) map performed on an undeformed sample; along with (g) the full LAM map using an 8° cut off. The black dashed boxes in (f) give examples of where 2 α variants are sampled by a single kernel, giving false data. (For interpretation of the references to colour in this figure legend, the reader is referred to the web version of this article.)

low strain regions. The effect of increasing this misorientation filter is depicted in Fig. 1f, where the range allowed has been increased to 8°. It can be seen that, in this case, the sampled pixel set orientations (boxes in Fig. 1f) are introducing a second variant. This effect is also detected in the LAM kernel results in Fig. 1g, where artificially higher local misorientations are reported near the variant boundaries.

In summary, performing LAM measurements with pre-filtering to first segment single α variants allows large maps to be obtained, that can

capture the build-up in misorientations in the α phase with plastic strain. However, they are quite constrained in the misorientation range in which they can provide reliable data because, during plastic deformation when strain gradients within a single α variant exceed 5°, they cannot be uniquely identified and have to be filtered out of the results. In addition, the undeformed starting material also contains small misorientations which will influence the lowest strain that can be measured. Finally, the LAM measurements do not directly measure plastic strain, but the increase in crystallographic misorientation across a family of α variants that occurs due to local orientation gradients, generated by the plastic deformation. To interpret this measurement in the form of a plastic strain, therefore, requires a physical model or, more simply, calibration against identical microstructures subjected to a known plastic strain developed with a similar strain tensor.

3. Results

3.1. PSC calibration samples

In order to quantify the strain distributions found in Ti64 inter-pass rolled WAAM components, samples with a known strain were required to calibrate the α LAM measurements that had been deformed with a similar deformation mode. This was achieved by compressing 5 mm^3 cubic WAAM samples in a PSC rig (schematic shown in Fig. 2a). Fig. 2b shows an example optical image of a full PSC sample after deformation. Non-symmetric barrelling occurred during the PSC test due to dissimilar sliding friction between the PSC rig platen and the channel. However, this had the advantage of providing a strain gradient down the centre line from the partial dead zone at the top of the sample to the centre, which could be used to validate the EBSD-LAM measurements within a single specimen.

2.6 mm long, 0.35 mm wide EBSD strip maps were performed down the centreline of the PSC samples in the sample compression and expansion plane (TD-WD), to measure the local strain-induced misorientations in the α phase using the LAM technique described in §2.4. An original α-phase EBSD map taken from a sample compressed by 7.3% is shown in Fig. 3a and has been compared to the LAM map in Fig. 3b calculated from the EBSD data. In Fig. 3a, it should be noted that more mis-indexing has occurred in highly strained areas. The LAM data, averaged in the map-width direction, has also been plotted as a function of distance from the top of the same sample and compared to the FE simulations of the local effective strain in Fig. 4.

The bright and dark areas in the LAM map shown in Fig. 3b represent high and low local average misorientations, respectively. In Fig. 4 in the region starting from ~1.25 mm below the top of the sample, it can be seen that there is a near-linear correspondence between the LAM measurement and simulated local strain. A misorientation peak can also be seen at the sample's top surface, which is not reflected in the FE analysis, as a result of the immediate surface deformation caused by the PSC rig platen friction. In addition, in the distance range from ~0.5–1.25 mm from the top of the sample, the LAM data shows a minimum value of ~1.4°. This corresponds to the lower misorientation resolution limit of the LAM technique in a transformation microstructure, for the reasons discussed above (§2.4). This lower limit is mainly caused by the pre-existing small misorientations between the α lamellae that form during the β → α transformation [57–59]. Over a distance of 1.25–2.5 mm down the sample centre, the LAM measurements then increase and plateau near to the sample centre at ~3.5°, where one would expect the region of highest and most uniform strain to occur in the PSC test.

In the region of the strain gradient (i.e. 1.25–2.5 mm from the top of the PSC sample) to the central plateau (~ 3.5 mm below) averaged data was extracted every 0.25 mm, so that the LAM measurements could be plotted against the local strain calculated from the FE model. The comparative values from these measurements are summarised in Fig. 5a, where it can be seen that, in this limited range, there is a close to linear relationship between the α-phase LAM values and the simulated strain. However, for deformation strains above 12%, the LAM values saturate and no longer increase. A similar effect was also found in a sample compressed to a ~10% reduction ratio, which has not been included in Fig. 5a for clarity. We have not yet fully investigated why saturation of the LAM measurements occurs for higher strains, but it is probably caused mainly by the 5° pre-filter, which starts to exclude more intensely misorientated pixels from the kernel averaging as strain increases. This would be expected to be more problematic if slip starts to localise, which is known to occur in a WAAM material because of the fine-scale transformation microstructure and the combination of 'hard' and 'soft' orientations present with regard to the local strain direction [35,36]. At low strains, the LAM technique can also not resolve misorientation changes below 1.25°, which means the strain can only be accurately determined using this mapping approach in the range

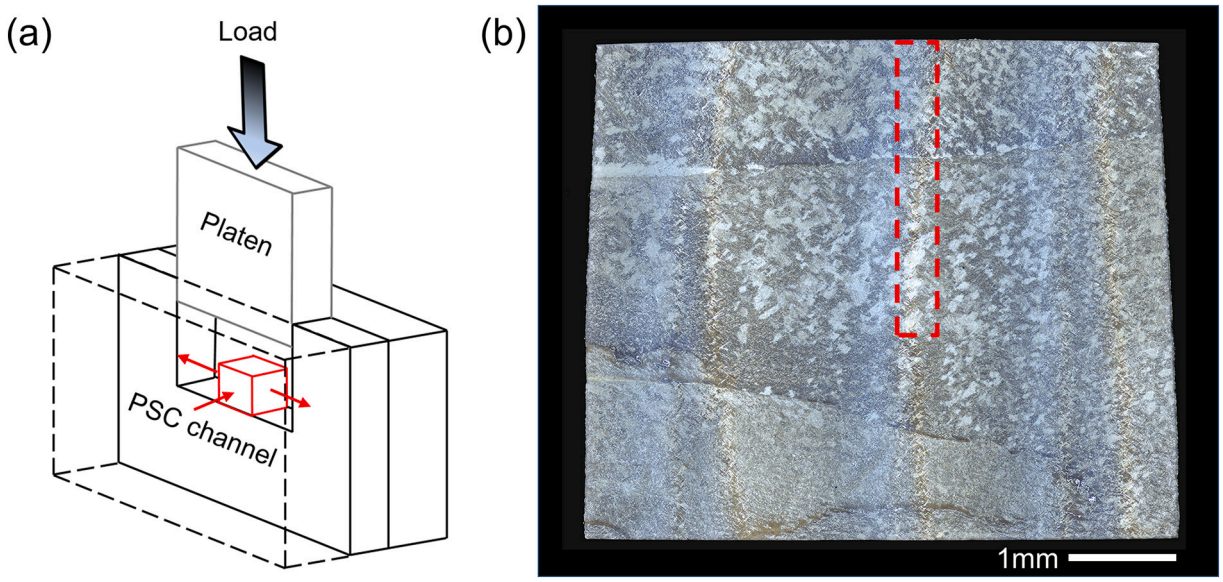

Fig. 2. (a) Schematic of the plane strain compression rig (adapted from [28]). (b) Example optical centre macro-section of a whole PSC sample subjected to a compression ratio of 7.3%. The red rectangle indicates the region analysed in Figs. 3–5. (For interpretation of the references to colour in this figure legend, the reader is referred to the web version of this article.)

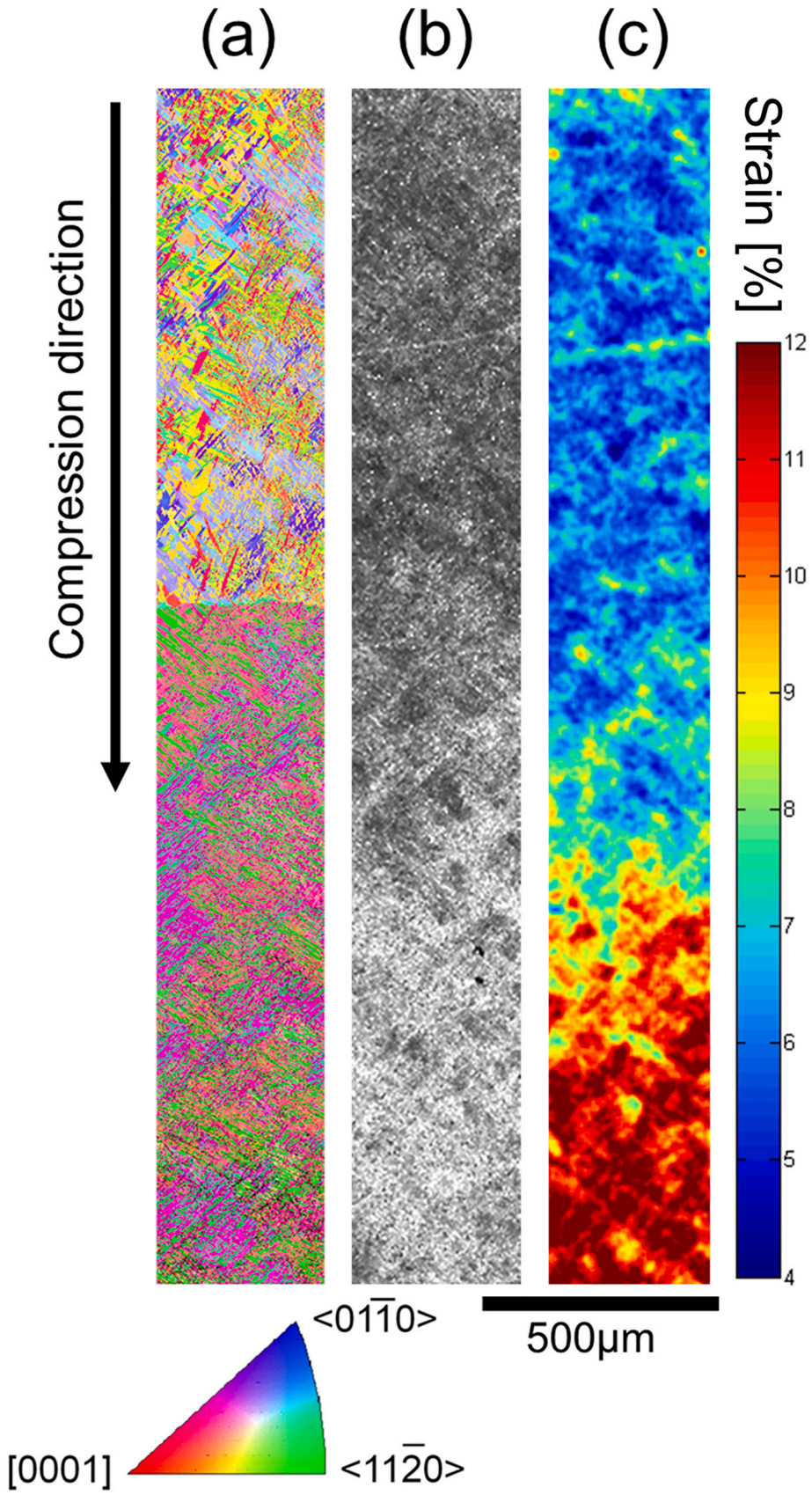

Fig. 3. EBSD maps of the PSC sample with 7.3% reduction: (a) raw EBSD data with IPF orientation colouring with respect to ND, where mis-indexed points indicate areas of high strain, (b) LAM map, and (c) a quantified strain map using the EBSD-LAM technique.

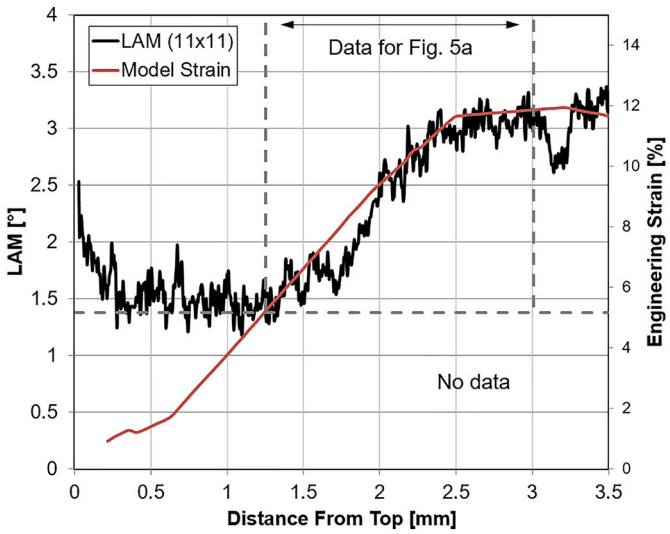

Fig. 4. EBSD-LAM line scan down the centre of a PSC sample compressed by 7.3%, plotted against the effective strain obtained from the FE model simulation of the PSC test. Note: no data was obtainable below the dotted line due to the sensitivity limit of the LAM technique.

between ~6–12%.

Although the strain range that can be quantified by this approach is limited, fortuitously, it is still sufficient to be very useful for studying the effect of surface deformation techniques on the rapid-heating β RX mechanism in WAAM. This is because, in previous work, where a process map for WAAM with inter-pass deformation was developed (Fig. 5b), it was found that recrystallization caused by rapid-heating β RX conveniently initiates for applied strains greater than ~9%, and the minimum grain size achieved by exploiting this mechanism saturates at strains greater than ~14% [25]. Despite the restricted strain range available, mapping the local strain by the EBSD-LAM technique can, therefore, still be used to predict the limits of a surface-induced plastic zone where the minimum strain has been achieved to induce rapid-heating β RX, and can also identify most of the region where there will be a grain size gradient.

3.2. Application of LAM strain mapping to rolled WAAM samples

The EBSD-LAM strain quantification technique was used to investigate the effectiveness of WAAM inter-pass surface rolling, on two separate roller tracks produced using down forces of 90 and 100 kN, to see if the effect of a small difference in the rolling load could be detected in the sub-surface strain distributions. The surface indent and sub-surface macro-structure beneath the 90 kN track is shown in Fig. 6a, along with microstructures seen at higher magnification within the roller strain field close to the surface in Fig. 6b–c, and the as-built microstructure far below the strain field is depicted in Fig. 6d. The etched optical image in Fig. 6a also reveals the large columnar prior β-grain structure and HAZ banding, typically found in WAAM samples (e.g. [7]). The fine α + β basket-weave transformation microstructure, which had an average α inter-lamellar spacing of ~0.9 μm [43], is shown in Fig. 6d. Within the deformation zone near the surface in Fig. 6b–c, it can be seen that the α lamellae have become distorted due to slip occurring heterogeneously within different variant orientations.

Large area EBSD α orientation maps were performed over ~4 × 3 mm areas across and below the 90 and 100 kN rolled tracks, using the conditions described above, and processed to calculate LAM maps, which were then replotted as effective strain maps using the linear correlation determined in Fig. 5a. The resultant smoothed LAM and contoured strain maps are compared in Fig. 7 for the 90 and 100 kN load tracks. It can be seen that in both cases, each strain field extends slightly wider than the roller contact profile and the strain is concentrated at the contact area edges, near the surface, and then extends downwards to produce a semi-circular region of high-strain below the surface. Directly below the centre of the roller, there is also a dead zone just below the surface. The depth to which the plastic strain field can be detected by the LAM method is considerable, being 3–4 mm, which is similar to the roller contact area width and much deeper than one deposited layer height, which is ~1–1.4 mm [8,43] in the WAAM process. Clear differences can also be detected between the strain maps obtained for the two tracks, despite the small increase in rolling load; i.e. the depth and intensity of the strain field is obviously greater in the 100 kN sample. The region within the highest detectable strain contour (above 12%) is also significantly larger for the 100 kN roll track, which implies that the larger rolling load will lead to a greater and more uniform RX region being formed on rapid re-heating.

In the 90 kN load rolled sample (Fig. 7a and c), the high-strain region reaches above the saturation limit of 12% strain near the sample surface, but ~2.5 mm farther down and towards the roller profile centreline, the strain drops to below 9%, beyond which no gain nucleation would be expected, according to the process map established in ref. [25], and reproduced in Fig. 5b. The strain field measured from the sample rolled with a 100 kN load (Fig. 7d) therefore infers that at least 12% strain is achieved at a depth of up to ~2 mm, and the strain is still above the 9% threshold required to produce new β orientations, on rapid re-heating, as deep as ~3 mm below the sample surface, although a small less deformed 'dead' zone is also seen below the roller profile centreline at the surface to a depth of 0.2 mm. Therefore, in this sample, following rolling and rapid re-heating, β RX would be expected to occur to a depth of ~3 mm below the surface, and an approximately uniform grain size would be predicted across three quarters of the rolled profile, up to a depth of at least 2 mm. In Fig. 7b, the 100 kN load strain field also appears to have a sharper strain gradient towards the field edges, when compared to the strain field for the 90 kN load sample (Fig. 7a), but this may be a false impression caused by the inability to resolve high strains within the sample.

3.3. β annealing and 'rapid-heating β RX'

After the rolled samples were mapped by EBSD and their strain fields quantified, they were rapidly heated above the β transus temperature to ~1175 °C at a rate of ~600 °C s^{-1}, to simulate the thermal cycle in the WAAM process [43] and induce rapid-heating β RX. β-reconstructed EBSD maps from these samples (showing equivalent areas to in Fig. 7) are provided in Fig. 8. In this figure, it can be clearly observed that the coarse columnar β-grain structures have been greatly refined in the plastic zones below the roller contact area into relatively small, equiaxed grains, separated mostly by HAGBs (coloured black in the EBSD maps in Fig. 8). The RX grains from these maps have also been coloured by grain size binning in Fig. 9 to better illustrate the variation in the β-RX region, between the two samples. Compared to the 100 kN sample, in the plastic zone from the 90 kN roll track, the β-grain sizes are less uniform but a high level of grain refinement still occurred within the semi-circular high-strain area, where the effective strain was measured to be ~12% (Fig. 7c). In contrast, more uniform refinement was observed across the plastic zone in the 100 kN rolled sample (Figs. 8b and 9b), although the minimum grain size was similar in both cases. This grain size distribution agrees with the larger high-strain region seen at the edge of the plastic zone, detected by EBSD-LAM mapping in the sample produced with the greater rolling load in Fig. 7d. Additionally, the grains at the edge of the plastic zone in the 90 kN sample can be seen to have grown outwards more into the surrounding less strained region, causing them to elongate [21]. This behaviour is less obvious within the deformation field for the higher rolling load condition, but some local areas of grain elongation can still be seen near the interface with the un-recrystallized surrounding material. Although no new grain nucleation is expected where the strain level falls below 9% (Fig. 5b), the stored energy in

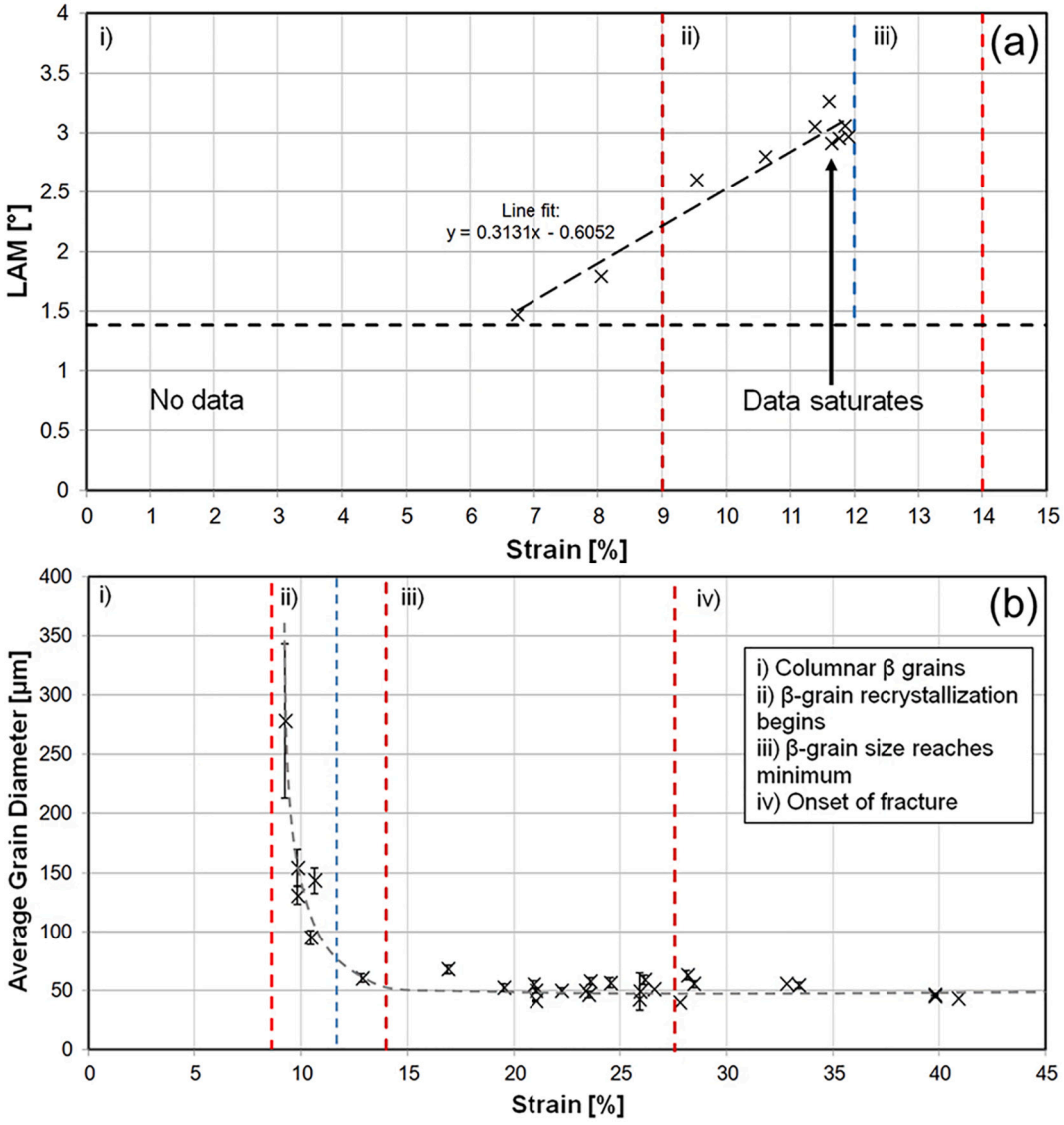

Fig. 5. (a) EBSD-LAM measurements plotted against the local strain in PSC samples, determined by FE simulation, taken at 0.25 mm intervals down the sample centre in a 7.3% compressed sample, compared to (b) the effect of strain on grain refinement in PSC WAAM samples subject to rapid heating, reproduced from [25]. Note: the x-axis strain scales are different.

material volumes that experienced lower strains has been found previously to be still sufficient to promote outward growth of new β-grain orientations formed in more highly strained regions [21,25]. Thus, these results confirm there was probably a less steep strain gradient at the edge of the plastic zone in the 90 kN sample than with the 100 kN rolling load (Fig. 7), as a shallower gradient would allow the RX grains to elongate more by directional growth.

There are also some larger grains present in the semi-circular highly strained region within the deformation zone of the 100 kN sample – which are highlighted in Fig. 9b (marked (i) and (ii)). When examined more closely, it can be seen that these are actually areas containing mainly subgrains separated by low angle grain boundaries (LAGBs) which are highlighted in white in Figs. 9 and 10. The subgrains are of similar size to the surrounding more highly misorientated grains. Interestingly, when compared to the strain map in Fig. 7b, the region where these less refined grains were found coincided with the most highly strained area of the plastic zone.

The reconstructed β phase pole figures displayed in Fig. 11 compare the strong $<001>_\beta$ // ND orientation of the parent columnar β-grains from the undeformed region of the 100 kN rolled sample (Fig. 11a) to that in the RX region within the roller's plastic strain field (Fig. 11b). From comparison of the $\{001\}_\beta$ pole figures, it can be seen that the RX region contains one strong orientation (marked (i)) of ~6 MRD intensity, and another less strong orientation (ii). Both of these orientations are in similar *relative* positions to the two parent β-grain texture poles seen in Fig. 11a. However, they have rotated away from their original position by ~10° around ND. If these two stronger components are separated out, the remainder of the new orientations can be seen to surround the stronger original position of the parent $<001>_\beta$ pole with a 'square' four-fold intensity distribution, with corners located about ~20–30° from the parent grain $<001>_\beta$ pole. Interestingly, these two texture features also correspond to two types of microstructure: the stronger single poles, marked (i) and (ii) in the $\{001\}_\beta$ pole figure in Fig. 11b, corresponding to the original parent β-grain orientations, originating from the subgrain regions highlighted in Fig. 10, whose separated textures are also shown in Fig. 10i and ii. Thus, when considered together, it is evident that these retained subgrain regions are surviving grain fragments that have not been consumed by recrystallization and rotated away from their respective bulk columnar parent grain $<001>_\beta$ orientations (seen in Fig. 11a). In addition, the remaining

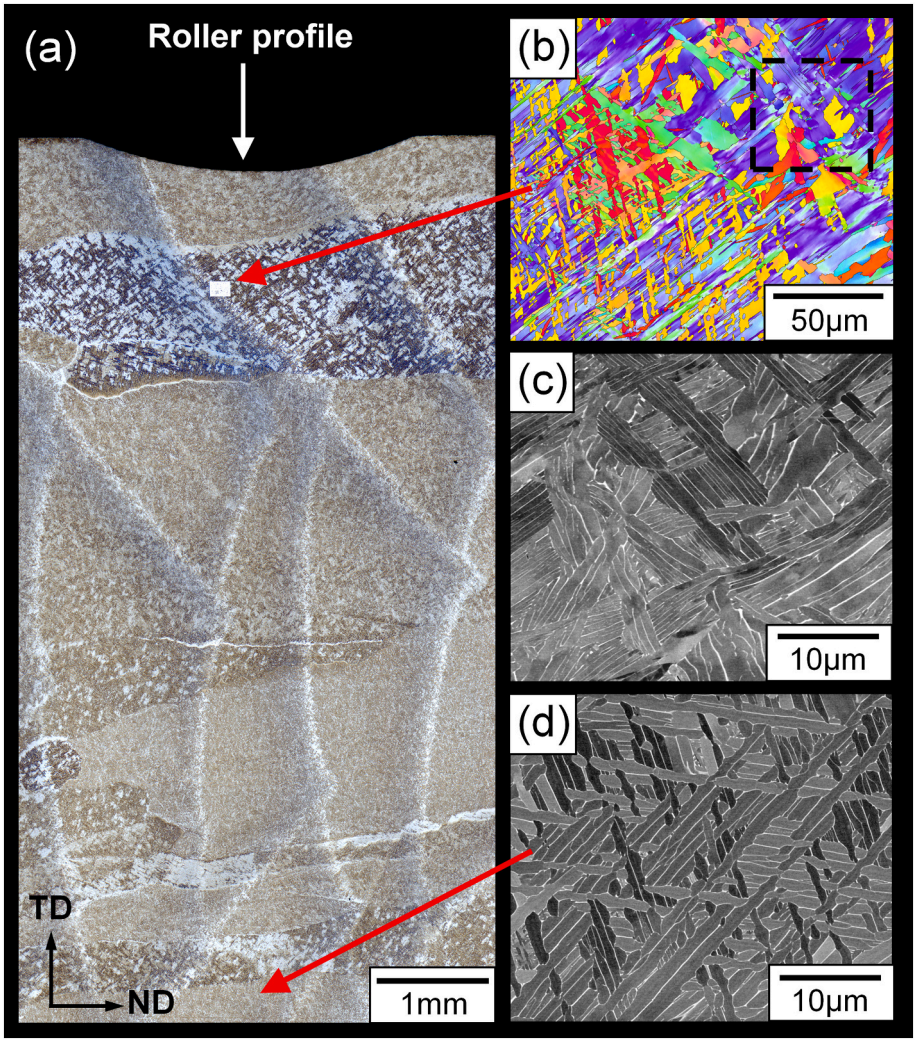

Fig. 6. Macro images and micrographs from the WAAM 90 kN load rolled samples sub-surface region (before rapid heating): (a) etched optical image showing the as-deposited structure and the imparted roller profile, (b) EBSD map of the deformed α microstructure within the roller strain field close to the surface, (c) SEM-BSE micrograph of the region indicated in (b) (dashed square); and (d) SEM-BSE micrograph from the as-deposited strain-free microstructure far from the rolled surface.

part of the intensity distribution seen in the $\{001\}_\beta$ pole figures, which corresponds to that of the new RX grains, has a distribution with a four-fold motif arranged symmetrically around the strong $<001>_\beta$ parent pole seen in Fig. 11a. This intensity distribution is very similar to the four-fold $\{001\}_\beta$ texture motif characteristically produced by the rapid-heating β RX mechanism, reported previously by the current authors [25,28], but is less regular than the ideal distribution seen in previous texture measurements, which is not surprising given the more complex and non-uniform deformation field produced by a contoured roller. The more idealised distribution of this texture intensity is shown in Fig. 11c, for comparative purposes, which was obtained by rapidly heating a single parent β grain that had been subjected to a plane-strain compression of 14% [28].

4. Discussion

Introducing an inter-pass deformation step to single-track-wide wall deposits has previously been shown to be very effective at breaking up the coarse columnar β-grain structures found in the WAAM process, with Ti64, and for producing refined β equiaxed grains throughout a component [7,8,19]. A recent investigation, that physically simulated the deformation and rapid heating conditions present in the WAAM process, has also demonstrated that the RX mechanism that produces new β-grain orientations becomes active at a minimum applied strain level of ~9%, and saturates at strains above ~14%, with a further increase in strain producing no more reduction in grain size [25]. This work has also shown that the main RX mechanism itself may well be specific to AM processes, and results from a favourable set of circumstances that involves the effect of light deformation on the subsequent re-growth behaviour of the β phase, when a fine-scale α lamellar transformation structure is deformed and re-heated rapidly through the β transus [21,25,28]. Our previous simulation investigation showed that this results in a characteristically unique β micro-texture forming within each parent β grain (exemplified by Fig. 11c) which may be being formed by the retained β phase twinning during its re-growth, due to stacking faults arising from defects created in the α-β interface by the prior deformation.

The current work was carried out to explore the potential for grain refining thicker section WAAM components than previously studied, by surface rolling added layers, using a small width contoured roller to create multiple overlapped deformation tracks, and thereby limit the mechanical loads required [24]. Here, the individual tracks have been studied to see if their deformation zones could be accurately measured by a practical microscopy technique and related to the degree and depth of grain refinement. While it has been found that the EBSD-based LAM technique can only be correlated to plastic strain in a limited range, it

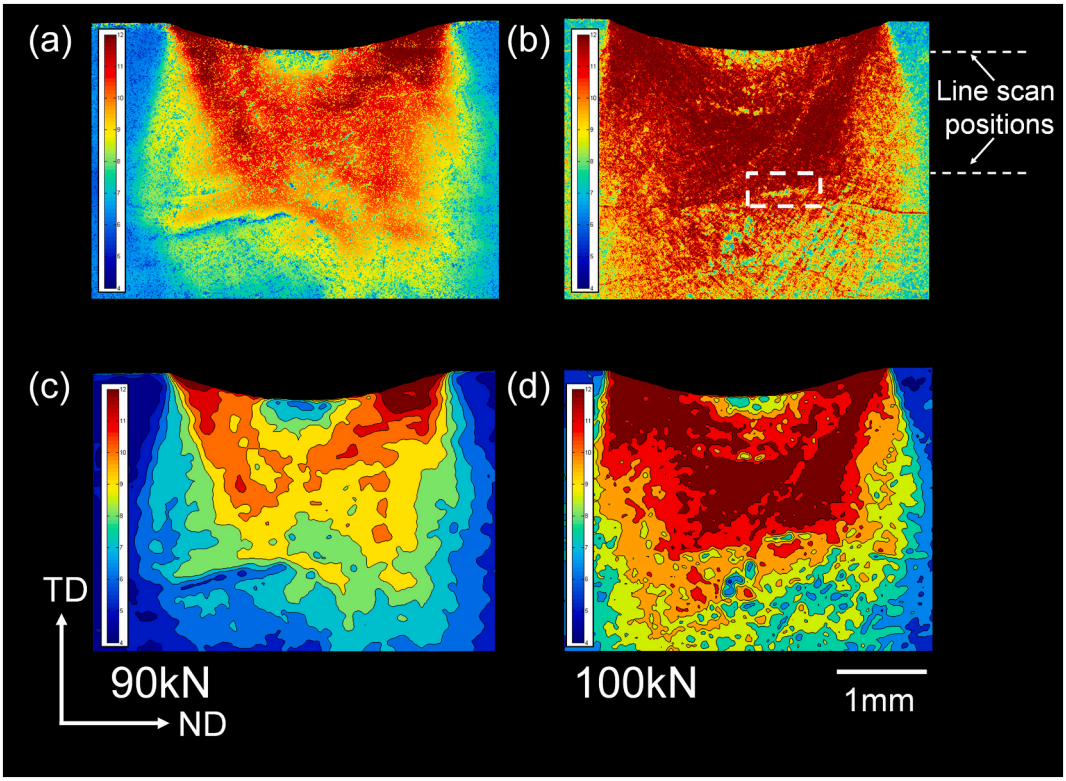

Fig. 7. EBSD-LAM strain mapping of the WAAM contoured roll tracks, produced with (a, c) a 90 kN and (b, d) a 100 kN load, showing the misorientation distributions obtained by the EBSD-LAM technique and the effective plastic strains estimated by calibration with the PSC samples. This data is shown as smoothed continuous (a-b) and (c-d) contoured data, respectively. The dashed white box highlights an area of heterogeneity caused by a prior columnar β-grain boundary, and the dotted white lines show the depth location of the strain line profiles depicted in Fig. 13.

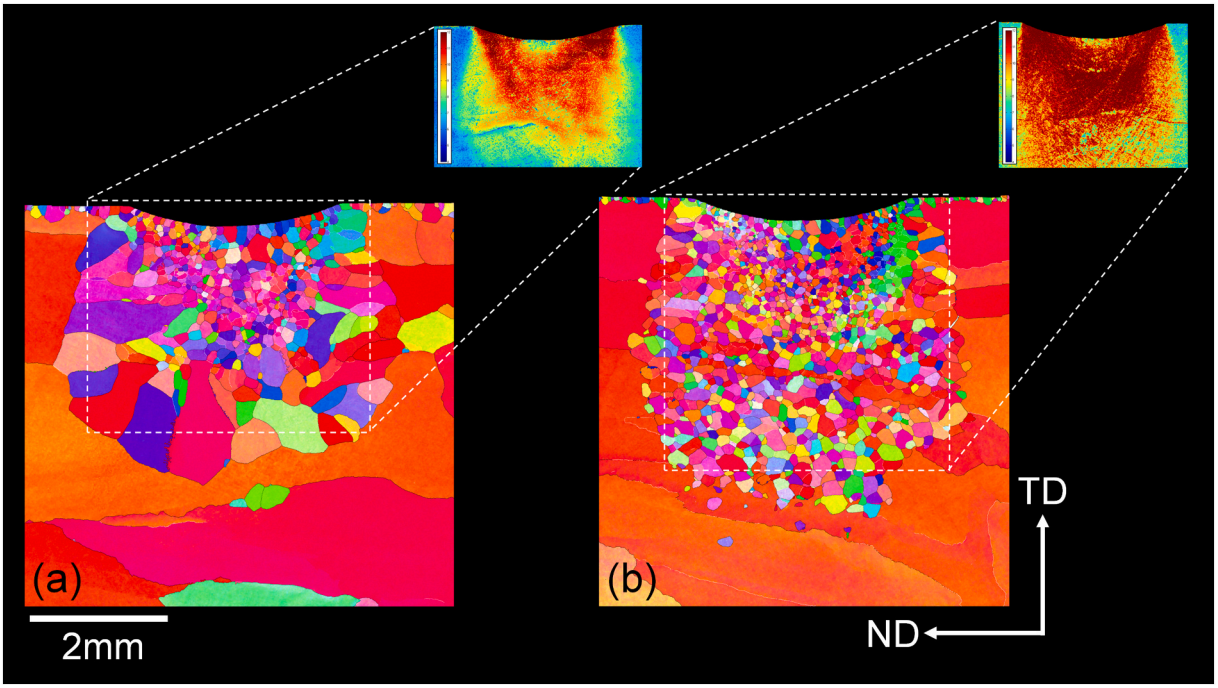

Fig. 8. Reconstructed β-phase maps after rapid β annealing, taken from the cold rolled samples using an (a) 90 kN and (b) 100 kN load. The areas relating to the strain maps measured for each sample (Fig. 7) are highlighted by the white dotted outlines. The EBSD maps are in IPF colouring relative to the build normal direction (ND).

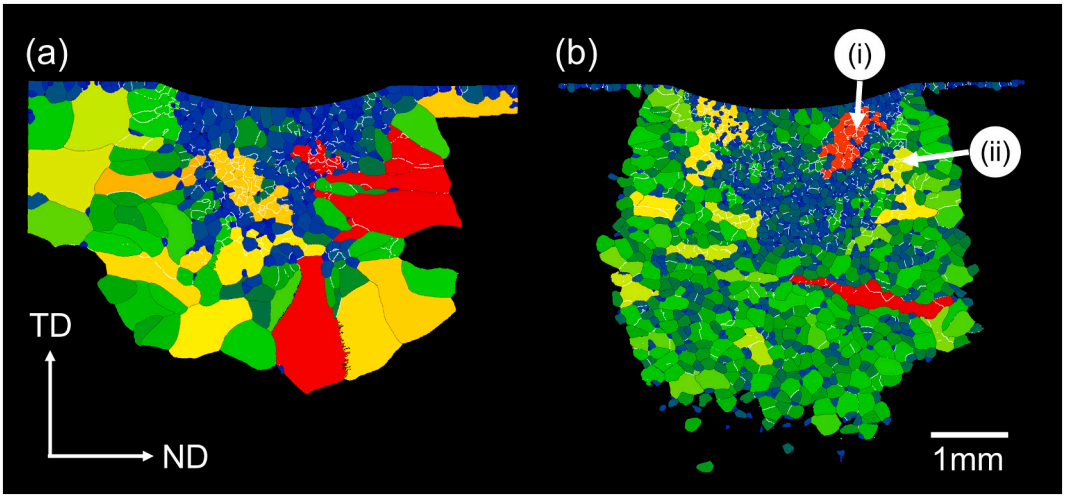

Fig. 9. Reconstructed-β EBSD grain size maps with the grains distinguished using a misorientation above 15°, and coloured according to size range from the samples rolled with: (a) a 90 kN load and (b) a 100 kN load. High and low angle grain boundaries are coloured black and white, respectively. (i) and (ii) highlight regions of high strain where subgrain structures still dominate, the texture of which are shown in higher resolution EBSD maps in Fig. 10.

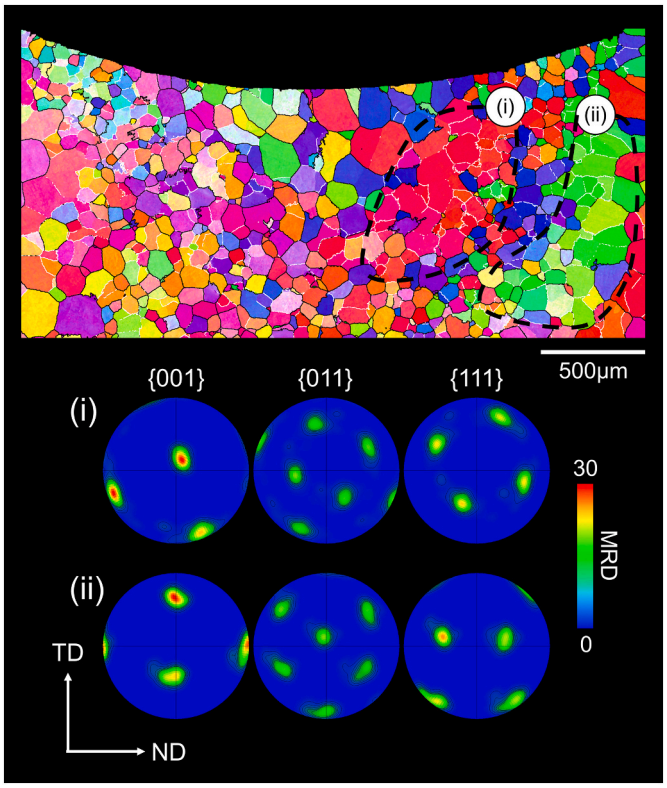

Fig. 10. EBSD map showing the area close to the surface of the 100 kN rolled sample in higher resolution. The map is in IPF colouring relative to the WAAM build direction (ND). The regions highlighted (i) and (ii) contain subgrain colonies separated by LAGBs (coloured white). The micro-textures from region (i) and (ii) are presented in the β pole figures below.

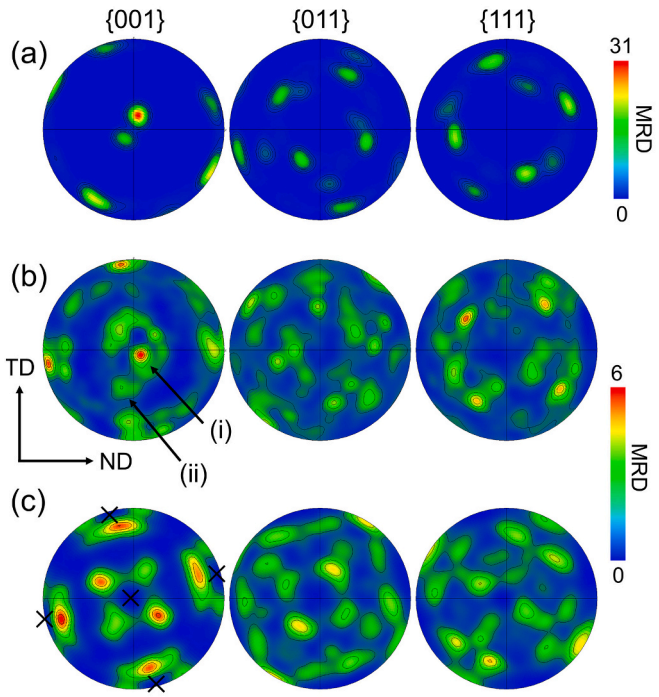

Fig. 11. Pole figures showing the β-phase textures found in the rapidly β-annealed WAAM sample in the region of the 100 kN contoured roller track: (a) orientations of the surrounding matrix that were dominated by one strong and one weaker parent grain orientation, and (b) the RX region only. The poles labelled (i) and (ii) correspond to the strong intensities from the subgrain regions shown in Fig. 10 (their separated textures are also given in the pole figures in Fig. 10i and ii). (c) shows the ideal unique β RX texture found on rapidly re-heating a deformed single parent β grain, following uniform PSC (taken from [28]). The positons of the original parent grain {001} poles are also indicated in (c) by crosses. Note: the texture strengths have been re-scaled, owing to the much weaker texture present in the RX region.

has still been shown to be a very useful method for characterizing the plastic zone size and area that recrystallizes during rapid re-heating, with good agreement seen between the strain mapping and the reconstructed-β EBSD maps after β annealing. In addition, there are currently limited alternative options for trying to map plastic strain fields in an extremely fine-scale α lamellar microstructure over a practically useful, large length scale. An obvious alternative is to use hardness mapping. A direct comparison is made in Fig. 12 between the LAM method and an automated micro-hardness map produced with a 150 μm step size, using an applied load of 0.1 kg on the 90 kN rolled sample. In comparison to the LAM strain mapping technique, the hardness map is extremely poor at defining the plastic strain field, or the depth of deformation, which is particularly badly resolved.

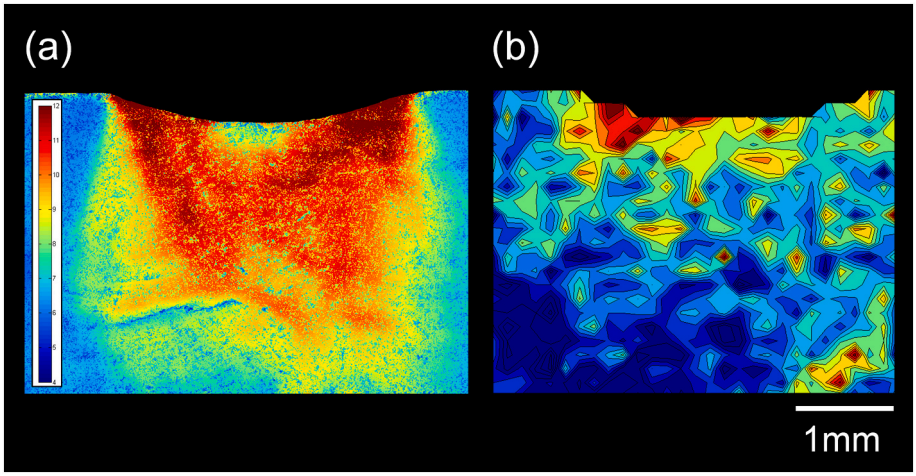

Fig. 12. Comparison between the plastic strain distribution induced by surface rolling, interpreted by (a) the EBSD-LAM mapping technique and (b) conventional micro-hardness mapping, performed on the 90 kN load rolled sample.

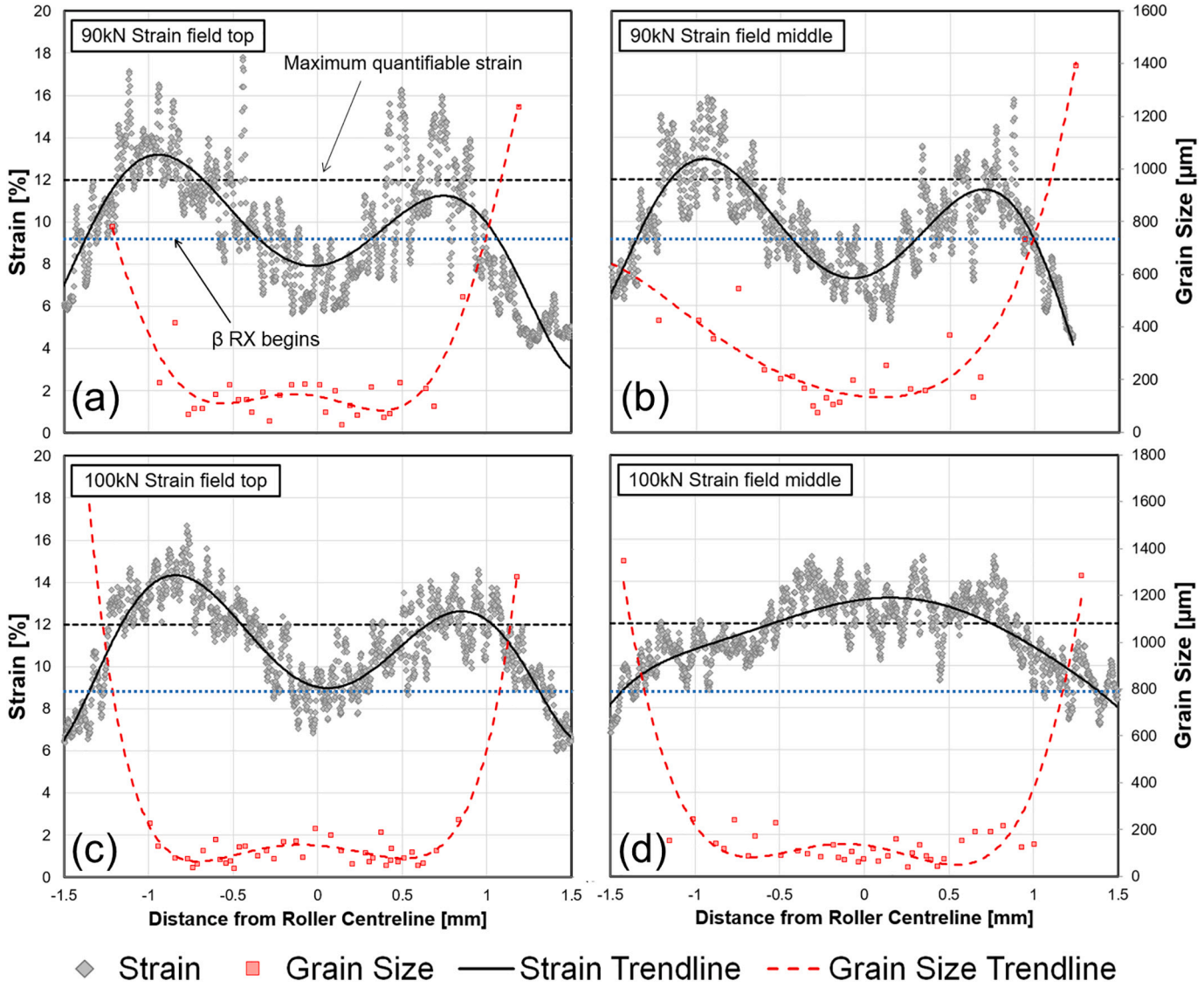

Fig. 13. EBSD-LAM strain and RX β-grain size profiles, plotted as a function of distance from the roller position centreline for the 90 kN load rolled sample, across (a) the top and (b) the bottom of the plastic zone; and also for the 100 kN load rolled sample, (c) top and (d) bottom. The locations used for the profiles are shown in Fig. 7. The strain and grain size data has been fitted with polynomial best fit lines.

The strain maps produced using the EBSD-LAM technique for the 90 and 100 kN load rolled samples (Fig. 7a and b, respectively) reveal a semi-circular strain field that also matches closely to the profiles predicted from FE models by Abbaszadeh et al. [47]. Although this work focused on modelling rolling the top of a less-constrained, narrower, single-track-wide wall, it shows a similar strain distribution to that found with the EBSD-LAM technique, with a dead zone developing directly under the roller contact footprint and a semi-circular high strain region being apparent, connecting from the edges of roller contact to a depth below the roll centreline of 1 mm. The FE modelling, however, predicted a maximum plastic strain of the order of 30% with a similarly profiled (3 mm radius) roller, which is beyond the saturation limit of the LAM method.

For the results presented here, the large difference seen between the deformation fields generated by the 90 and 100 kN rolling loads are also explained by the low strain hardening rate of the WAAM deposited Ti64 material, which has a relatively high yield stress owing to the fine transformation microstructure present in this material. In the EBSD-LAM strain maps, the 100 kN load sample appeared to produce a more homogeneous strain field than that seen with a 90 kN rolling load, although this did not seem to result in higher strains. However, this is probably an artefact caused by saturation of the misorientation level measured with plastic strain, which occurs at ~12%; particularly given that the FE simulations of Abbaszadeh et al. [47] suggest higher maximum strains should be expected (~ 30%).

Strain profiles taken across the maps in Fig. 7, from near the 90 and 100 kN rolled sample surfaces and 2 mm below, are provided in Fig. 13 (the line scan depth positions are indicated in Fig. 7). The profiles have been fitted with polynomial best fit lines, as there was significant local scatter due to local variation in the misorientation data and EBSD stitching errors. In this graph, we have also plotted the corresponding RX β-grain sizes, shown in Figs. 8 and 9. In Fig. 13, both rolled samples show dual strain peaks corresponding to the semi-circular maximum strain distribution seen in Fig. 7 and also exhibit RX grain sizes following the same pattern as the strain measurements (Fig. 13a, b, and c); i.e. the positions of the highest strain peaks correspond approximately to the smallest grain size. The data also suggests that, when comparing the line scans of the samples' central regions, there was greater homogeneity in the strain field in the 100 kN load sample, where the 90 kN strain plot (Fig. 13b) exhibits dual peaks. The 100 kN load plot (Fig. 13d) displayed only a small change in strain across the plastic field with a steady increase towards the roller centreline; but, as noted above, the peak strains reached are likely to be higher than the saturation limit of the EBSD-LAM technique, and will therefore tend to be artificially flattened out more for the case of the higher rolling load.

Overall, therefore, in the fine-scale Ti64 α + β transformation microstructures produced by the WAAM process, the EBSD-LAM strain mapping technique has been successful in correctly identifying regions where the rapid-heating β RX mechanism will be activated and produce regions of highly misorientated, refined, equiaxed grains. In addition, it has also revealed lesser strained regions where grain nucleation does not occur, but that new RX grains are able to grow into. However, due to the fundamental limits of the EBSD-LAM measurement, the quantifiable strain saturated at 12%, and thus highly strained regions were not interpretable by this method.

Previous investigations have demonstrated that the rapid-heating β RX mechanism activates at plastic strains above ~9% [7,8,25], and the EBSD-LAM strain quantifying technique predicted this behaviour correctly, as can be seen in Fig. 13 where, as the strain approached 9% (marked with the blue dotted line) the grain size rapidly reduced and then plateaued as the strain exceeded 12%. However, when studying the single contoured roll tracks, some significant local heterogeneities were also observed. For example, the 90 kN load rolled sample differed from the 100 kN, in that it displayed more significant β-grain growth at the edge of the RX area, which is indicative of a lower strain gradient at the periphery of the plastic zone, with a wider surrounding region being present below the strain limit required for grain nucleation [21,25]. Since such extensive directional grain growth did not occur in the 100 kN load rolled sample (Fig. 8b), this suggests that there was a sharper strain gradient at the edge of its plastic zone, which is also evident in the strain maps in Fig. 7 and strain profiles in Fig. 13. Retained coarser β-grain regions were also found to be present in areas where the maximum strain was located, particularly in the track produced by the higher rolling load. In these regions, which correlated to areas below the edge of the roll contact, the micro-texture could be related to a sample rotation form the parent β grain, which suggests that, locally, less rapid-heating β RX had occurred, and another mechanism may be dominant where the highest local shear strains would be expected [60].

In the two rolled samples studied in this work, three β RX features have, therefore, been identified, which correlate to different levels of local strain: i) above 9% strain where fine-grained regions were found that had a characteristic micro-texture indicative of the rapid-heating β RX mechanism (previously discussed [7,8,25,28]); ii) regions at the edge of the plastic zone where the strain was less than 9% with a strain gradient to the surrounding undeformed matrix, where only directional grain growth occurred from new orientations generated in the centre of the more strained plastic zone by the aforementioned rapid-heating β RX mechanism, and where the driving force for growth diminished with distance as the strain approached zero; and iii) regions of high local shear (probably > ~30%) below the edge of the roller contact footprint, where some coarser rotated β-grain fragments survived, or conventional RX had occurred of new grains within the orientation spread generated by the high shear strain [60].

5. Conclusions

Inter-pass deformation, or 'incremental-forging', is a useful method for refining the coarse primary β-grain structures normally produced in high deposition rate AM processes, like WAAM with Ti alloys. However, it is more difficult to apply such deformation-based techniques to strong alloys and thicker section parts. The potential of one approach to refining larger sections has been investigated, which involves using a radiused contoured roller to apply translated overlapping deformation tracks to each added layer. Here, we have attempted to measure the plastic zone size and strain distribution generated by individual roller tracks, which is a fundamental requirement for optimising such a process, and relate the strain distribution to the level of grain refinement and the recrystallization mechanisms that occurred on re-heating at high heating rates, that simulated the thermal cycle generated when the next layer is added in the WAAM process.

Although the EBSD-based LAM technique employed could only be correlated to a quite limited range of plastic strain, it was found to be a much more effective method than alternative approaches, such as microhardness mapping, and was still successful in defining the plastic zone size and area that recrystallized during rapid re-heating.

LAM-strain mapping has shown that, due to the low strain hardening rate of a WAAM Ti64 material, there is a high sensitivity of the rolling pressure to the depth and intensity of the sub-surface plastic zone. The plastic zone itself has a 'dead zone' near the contact surface and a region of more intense shear, forming a semi-circular pattern emanating from the edge of the contact footprint of the roller. Good agreement was found between the LAM strain maps and comparable published FE studies.

Data availability

The raw/processed data required to reproduce these findings cannot be shared at this time due to technical or time limitations.

Declaration of Competing Interest

The authors declare that they have no known competing financial

interests or personal relationships that could have appeared to influence the work reported in this paper.

Acknowledgements

The authors are appreciative of the EPSRC's, UK (grants NEWAM – EP/R027218/1; LightForm – EP/R001715/1), Innovate UK, UK (Open Architecture Additive Manufacturing, OAAM) and AMAZE project (no. 313781) for supporting aspects of this research. The authors thank J. Donoghue for contributing Fig. 2a. P.B. Prangnell is also grateful to the Royal Academy of Engineering, UK, and Airbus for supporting this research through the Airbus-University of Manchester Centre for Metallurgical Excellence.

References

[1] S.W. Williams, F. Martina, A.C. Addison, J. Ding, G. Pardal, P.A. Colegrove, Wire + arc additive manufacturing, Mater. Sci. Technol. 32 (7) (2015) 641–647, https://doi.org/10.1179/1743284715y.0000000073.
[2] T. Duda, L.V. Raghavan, 3D metal printing technology, IFAC-PapersOnLine 49 (29) (2016) 103–110, https://doi.org/10.1016/j.ifacol.2016.11.111.
[3] J. Allen, An investigation into the comparative costs of additive manufacture vs. machine from solid for aero engine parts, Proc. Meet. RTO-MP-AVT 139 (2006) 1–10, https://doi.org/10.14339/RTO-MP-AVT-139-17.
[4] C. Körner, Additive manufacturing of metallic components by selective electron beam melting – a review, Int. Mater. Rev. 61 (5) (2016) 361–377, https://doi.org/10.1080/09506608.2016.1176289.
[5] T. DebRoy, et al., Additive manufacturing of metallic components – process, structure and properties, Prog. Mater. Sci. 92 (2018) 112–224, https://doi.org/10.1016/j.pmatsci.2017.10.001.
[6] M.J. Bermingham, D.H. StJohn, J. Krynen, S. Tedman-Jones, M.S. Dargusch, Promoting the columnar to equiaxed transition and grain refinement of titanium alloys during additive manufacturing, Acta Mater. 168 (2019) 261–274, https://doi.org/10.1016/j.actamat.2019.02.020.
[7] J. Donoghue, A.A. Antonysamy, F. Martina, P.A. Colegrove, S.W. Williams, P. B. Prangnell, The effectiveness of combining rolling deformation with wire-arc additive manufacture on β-grain refinement and texture modification in Ti-6Al-4V, Mater. Charact. 114 (2016) 103–114, https://doi.org/10.1016/j.matchar.2016.02.001.
[8] F. Martina, S.W. Williams, P.A. Colegrove, Improved microstructure and increased mechanical properties of additive manufacture produced Ti-6Al-4V by interpass cold rolling, SFF Symp. (2013) 490–496, https://doi.org/10.1007/s13398-014-0173-7.2.
[9] F. Martina, P.A. Colegrove, S.W. Williams, J. Meyer, Microstructure of Interpass rolled wire + arc additive manufacturing Ti-6Al-4V components, Metall. Mater. Trans. A Phys. Metall. Mater. Sci. 46 (12) (2015) 6103–6118, https://doi.org/10.1007/s11661-015-3172-1.
[10] P.A. Kobryn, S.L. Semiatin, Microstructure and texture evolution during solidification processing of Ti-6A1-4V, J. Mater. Process. Technol. 135 (2–3 SPEC) (2003) 330–339, https://doi.org/10.1016/S0924-0136(02)00865-8.
[11] G. Lütjering, J.C. Williams, Titanium, Springer, 2007.
[12] F. Wang, S.W. Williams, P.A. Colegrove, A.A. Antonysamy, Microstructure and mechanical properties of wire and arc additive manufactured Ti-6Al-4V, Metall. Mater. Trans. A Phys. Metall. Mater. Sci. 44 (2) (2013) 968–977, https://doi.org/10.1007/s11661-012-1444-6.
[13] X. Zhang, F. Martina, J. Ding, X. Wang, S.W. Williams, Fracture toughness and fatigue crack growth rate properties in wire + arc additive manufactured Ti-6Al-4V, Fatigue Fract. Eng. Mater. Struct. 40 (5) (2017) 790–803, https://doi.org/10.1111/ffe.12547.
[14] P. Åkerfeldt, M.L. Antti, R. Pederson, Influence of microstructure on mechanical properties of laser metal wire-deposited Ti-6Al-4V, Mater. Sci. Eng. A 674 (2016) 428–437, https://doi.org/10.1016/j.msea.2016.07.038.
[15] H. Galarraga, R.J. Warren, D.A. Lados, R.R. Dehoff, M.M. Kirka, Fatigue crack growth mechanisms at the microstructure scale in as-fabricated and heat treated Ti-6Al-4V ELI manufactured by electron beam melting (EBM), Eng. Fract. Mech. 176 (2017) 263–280, https://doi.org/10.1016/j.engfracmech.2017.03.024.
[16] S. Mereddy, M.J. Bermingham, D.H. StJohn, M.S. Dargusch, Grain refinement of wire arc additively manufactured titanium by the addition of silicon, J. Alloys Compd. 695 (2017) 2097–2103, https://doi.org/10.1016/j.jallcom.2016.11.049.
[17] J.R. Kennedy, D. Daloz, B. Rouat, E. Bouzy, J. Zollinger, Grain refinement of TiAl alloys by isomorphic self-inoculation, Intermetallics 95 (December 2017) (2018) 89–93, https://doi.org/10.1016/j.intermet.2018.02.001.
[18] J.R. Kennedy, B. Rouat, D. Daloz, E. Bouzy, J. Zollinger, Effect of inoculant alloy selection and particle size on efficiency of isomorphic inoculation of Ti-Al, Mater. (Basel) 11 (5) (2018) 1–15, https://doi.org/10.3390/ma11050666.
[19] L. Neto, S.W. Williams, J. Ding, J. Hönnige, F. Martina, Advanced Surface Enhancement, Springer Singapore, Singapore, 2020.
[20] J.R. Hönnige, P.A. Colegrove, S.W. Williams, Improvement of microstructure and mechanical properties in wire + arc additively manufactured Ti-6Al-4V with machine hammer peening, Procedia Eng. 216 (2017) (2017) 8–17, https://doi.org/10.1016/j.proeng.2018.02.083.
[21] J.R. Hönnige, et al., The effectiveness of grain refinement by machine hammer peening in high deposition rate Wire-Arc AM Ti-6Al-4V, Metall. Mater. Trans. A 51 (2020) 3692–3703.
[22] J.R. Hönnige, P.A. Colegrove, S.W. Williams, Improvement of microstructure and mechanical properties in wire + arc additively manufactured Ti-6Al-4V with machine hammer peening, Procedia Eng. 216 (2017) 8–17, https://doi.org/10.1016/J.PROENG.2018.02.083.
[23] A.R. McAndrew, et al., Interpass rolling of Ti-6Al-4V wire + arc additively manufactured features for microstructural refinement, Addit. Manuf. 21 (March) (2018) 340–349, https://doi.org/10.1016/j.addma.2018.03.006.
[24] P.A. Colegrove, J. Donoghue, F. Martina, J. Gu, P.B. Prangnell, J.R. Hönnige, Application of bulk deformation methods for microstructural and material property improvement and residual stress and distortion control in additively manufactured components, Scr. Mater. 135 (2017) 111–118, https://doi.org/10.1016/j.scriptamat.2016.10.031.
[25] A.E. Davis, J.R. Kennedy, J. Ding, P.B. Prangnell, The effect of processing parameters on rapid-heating β recrystallization in inter-pass deformed Ti-6Al-4V wire-arc additive manufacturing, Mater. Charact. 163 (February) (2020), https://doi.org/10.1016/j.matchar.2020.110298.
[26] ASM International, Materials Properties Handbook: Titanium Alloys, Materials Park, OH, 1994.
[27] S.L. Semiatin, An overview of the thermomechanical processing of alpha/beta titanium alloys: current status and future research opportunities, Metall. Mater. Trans. A (Figure 1) (2019) 1–102, https://doi.org/10.1007/s11661-020-05625-3.
[28] J. Donoghue, et al., On the observation of annealing twins during simulating β-grain refinement in Ti-6Al-4V high deposition rate AM with in-process deformation, Acta Mater. 186 (2019) 229–241, https://doi.org/10.1016/j.actamat.2020.01.009.
[29] D. Lunt, et al., Comparison of sub-grain scale digital image correlation calculated using commercial and open-source software packages, Mater. Charact. 163 (February) (2020), 110271, https://doi.org/10.1016/j.matchar.2020.110271.
[30] J. Carroll, W. Abuzaid, J. Lambros, H. Sehitoglu, An experimental methodology to relate local strain to microstructural texture, Rev. Sci. Instrum. 81 (8) (2010), https://doi.org/10.1063/1.3474902.
[31] J.D. Carroll, W. Abuzaid, J. Lambros, H. Sehitoglu, High resolution digital image correlation measurements of strain accumulation in fatigue crack growth, Int. J. Fatigue 57 (2013) 140–150, https://doi.org/10.1016/j.ijfatigue.2012.06.010.
[32] X. Xu, et al., Identification of active slip mode in a hexagonal material by correlative scanning electron microscopy, Acta Mater. 175 (2019) 376–393, https://doi.org/10.1016/j.actamat.2019.06.024.
[33] K. Sofinowski, et al., In situ characterization of a high work hardening Ti-6Al-4V prepared by electron beam melting, Acta Mater. 179 (2019) 224–236, https://doi.org/10.1016/j.actamat.2019.08.037.
[34] F. Di Gioacchino, J. Quinta da Fonseca, Plastic strain mapping with sub-micron resolution using digital image correlation, Exp. Mech. 53 (5) (2013) 743–754, https://doi.org/10.1007/s11340-012-9685-2.
[35] D. Lunt, et al., Microscopic strain localisation in WAAM Ti-6Al-4V during uniaxial tensile loading, Proc. 13th World Conf. Titan. (2019).
[36] D. Lunt, et al., The effect of loading direction on strain localisation in wire arc additively manufactured Ti–6Al–4V, Mater. Sci. Eng. A 788 (2020) 1–15, https://doi.org/10.1016/j.msea.2020.139608.
[37] J.Q. Da Fonseca, P.M. Mummery, P.J. Withers, Full-field strain mapping by optical correlation of micrographs acquired during deformation, J. Microsc. 218 (1) (2005) 9–21, https://doi.org/10.1111/j.1365-2818.2005.01461.x.
[38] D. Lunt, J.Q. da Fonseca, D. Rugg, M. Preuss, Microscopic strain localisation in Ti-6Al-4V during uniaxial tensile loading, Mater. Sci. Eng. A 680 (October 2016) (2017) 444–453, https://doi.org/10.1016/j.msea.2016.10.099.
[39] T. Ben Britton, S. Birosca, M. Preuss, A.J. Wilkinson, Electron backscatter diffraction study of dislocation content of a macrozone in hot-rolled Ti-6Al-4V alloy, Scr. Mater. 62 (9) (2010) 639–642, https://doi.org/10.1016/j.scriptamat.2010.01.010.
[40] S.I. Wright, M.M. Nowell, D.P. Field, A review of strain analysis using electron backscatter diffraction, Microsc. Microanal. 17 (3) (2011) 316–329, https://doi.org/10.1017/S1431927611000055.
[41] A.J. Wilkinson, T. Ben Britton, Strains, planes, and EBSD in materials science, Mater. Today 15 (9) (2012) 366–376, https://doi.org/10.1016/S1369-7021(12)70163-3.
[42] P.D. Littlewood, T.B. Britton, A.J. Wilkinson, Geometrically necessary dislocation density distributions in Ti-6Al-4V deformed in tension, Acta Mater. 59 (16) (2011) 6489–6500, https://doi.org/10.1016/j.actamat.2011.07.016.
[43] A. Ho, H. Zhao, J.W. Fellowes, F. Martina, A.E. Davis, P.B. Prangnell, On the origin of microstructural banding in Ti-6Al4V wire-arc based high deposition rate additive manufacturing, Acta Mater. 166 (2019), https://doi.org/10.1016/j.actamat.2018.12.038.
[44] G.A. Sargent, K.T. Kinsel, A.L. Pilchak, A.A. Salem, S.L. Semiatin, Variant selection during cooling after beta annealing of Ti-6Al-4V ingot material, Metall. Mater. Trans. A Phys. Metall. Mater. Sci. 43 (10) (2012) 3570–3585, https://doi.org/10.1007/s11661-012-1245-y.
[45] D. Qiao, W. Zhang, T.Y. Pan, P. Crooker, S. David, Z. Feng, Evaluation of residual plastic strain distribution in dissimilar metal weld by hardness mapping, Sci. Technol. Weld. Join. 18 (7) (2013) 624–630, https://doi.org/10.1179/1362171813Y.0000000144.
[46] L. Neto, S.W. Williams, J. Ding, J. Hönnige, F. Martina, Mechanical properties enhancement of additive manufactured ti-6al-4v by machine hammer peening, Adv. Surf. Enhanc. 1st Int. Conf. Adv. Surf. Enhanc. 1 (2020) 121–132, https://doi.org/10.1007/978-981-15-0054-1.

[47] M. Abbaszadeh, et al., Numerical investigation of the effect of rolling on the localized stress and strain induction for wire + arc additive manufactured structures, J. Mater. Eng. Perform. 28 (8) (2019) 4931–4942, https://doi.org/10.1007/s11665-019-04249-y.
[48] J.R. Hönnige, Thermo-Mechanical Control of Residual Stress, Distortion and Microstructure in Wire + Arc Additively Manufactured Ti−6Al−4V, Cranfield University, 2018.
[49] H. Zhao, A. Ho, A.E. Davis, A.A. Antonysamy, P.B. Prangnell, Automated image mapping and quantification of microstructure heterogeneity in additive manufactured Ti6Al4V, Mater. Charact. 147 (July 2018) (2019) 131–145, https://doi.org/10.1016/j.matchar.2018.10.027.
[50] P.S. Davies, An Investigation of Microstructure and Texture Evolution in the Near-α Titanium Alloy Timetal 834, University of Sheffield, 2009.
[51] P.S. Davies, B.P. Wynne, W.M. Rainforth, M.J. Thomas, P.L. Threadgill, Development of microstructure and crystallographic texture during stationary shoulder friction stir welding of Ti-6Al-4V, Metall. Mater. Trans. A Phys. Metall. Mater. Sci. 42 (8) (2011) 2278–2289, https://doi.org/10.1007/s11661-011-0606-2.
[52] M. Humbert, N. Gey, The calculation of a parent grain orientation from inherited variants for approximate (b.c.c.-h.c.p.) orientation relations, J. Appl. Crystallogr. 35 (4) (2002) 401–405, https://doi.org/10.1107/S0021889802005824.
[53] N. Gey, M. Humbert, Specific analysis of EBSD data to study the texture inheritance due to the β→α phase transformation, J. Mater. Sci. 38 (6) (2003) 1289–1294, https://doi.org/10.1023/A:1022842712172.
[54] F.J. Humphreys, Grain and subgrain characterisation by electron backscatter diffraction, J. Mater. Sci. 36 (16) (2001) 3833–3854, https://doi.org/10.1023/A:1017973432592.
[55] E. Lee, R. Banerjee, S. Kar, D. Bhattacharyya, H.L. Fraser, Selection of α variants during microstructural evolution in α/β titanium alloys, Philos. Mag. 87 (24) (2007) 3615–3627, https://doi.org/10.1080/14786430701373672.
[56] B. Radhakrishnan, S. Gorti, S.S. Babu, Phase Field simulations of autocatalytic formation of alpha lamellar colonies in Ti-6Al-4V, Metall. Mater. Trans. A Phys. Metall. Mater. Sci. 47 (12) (2016) 6577–6592, https://doi.org/10.1007/s11661-016-3746-6.
[57] D. Bhattacharyya, G.B. Viswanathan, R. Denkenberger, D. Furrer, H.L. Fraser, The role of crystallographic and geometrical relationships between α and β phases in an α/β titanium alloy, Acta Mater. 51 (16) (2003) 4679–4691, https://doi.org/10.1016/S1359-6454(03)00179-4.
[58] D. Bhattacharyya, G.B. Viswanathan, H.L. Fraser, Crystallographic and morphological relationships between β phase and the Widmanstätten and allotriomorphic α phase at special β grain boundaries in an α/β titanium alloy, Acta Mater. 55 (20) (2007) 6765–6778, https://doi.org/10.1016/j.actamat.2007.08.029.
[59] X. Zheng, et al., Twinning and sequential kinking in lamellar Ti-6Al-4V alloy, Acta Mater. 181 (2019) 479–490, https://doi.org/10.1016/j.actamat.2019.10.010.
[60] A.E. Davis, A. Caballero, P.B. Prangnell, Confirmation of rapid-heating β recrystallization in wire-arc additively manufactured Ti-6Al-4V, Materialia 13 (June) (2020) 0–5, https://doi.org/10.1016/j.mtla.2020.100857.